Confocal Raman spectroscopic analysis of cross-linked ultra-high molecular weight polyethylene for application in artificial hip joints

Giuseppe Pezzotti
Kyoto Institute of Technology
Ceramic Physics Laboratory
Research Institute of Nanoscience
Sakyo-ku, Matsugasaki
Kyoto 606-8585, Japan

Tsuyoshi Kumakura
Kyoto Institute of Technology
Ceramic Physics Laboratory
Research Institute of Nanoscience
Sakyo-ku, Matsugasaki
Kyoto 606-8585, Japan
and
Tokyo Medical University
Department of Orthopaedic Surgery
Shinjuku-ku, 6-7-1 Nishishinjuku
Tokyo 160-0023, Japan

Kiyotaka Yamada
Kyoto Institute of Technology
Ceramic Physics Laboratory
Research Institute of Nanoscience
Sakyo-ku, Matsugasaki
Kyoto 606-8585, Japan

Toshiyuki Tateiwa
Kyoto Institute of Technology
Ceramic Physics Laboratory
Research Institute of Nanoscience
Sakyo-ku, Matsugasaki
Kyoto 606-8585, Japan
and
Tokyo Medical University
Department of Orthopaedic Surgery
Shinjuku-ku, 6-7-1 Nishishinjuku
Tokyo 160-0023, Japan

Leonardo Puppulin
Wenliang Zhu
Kyoto Institute of Technology
Ceramic Physics Laboratory
Research Institute of Nanoscience
Sakyo-ku, Matsugasaki
Kyoto 606-8585, Japan

Kengo Yamamoto
Tokyo Medical University
Department of Orthopaedic Surgery
Shinjuku-ku, 6-7-1 Nishishinjuku
Tokyo 160-0023, Japan

Address all correspondence to Giuseppe Pezzotti, Department of Materials, Kyoto Inst. of Technology, Sakyo-ku, Matsugasaki-Sakyo-ku, Kyoto 606-8585, Japan; Tel: 81-75-724-7568; Fax: 81-75-724-7568; E-mail: pezzotti@ipc.kit.ac.jp

Abstract. Confocal spectroscopic techniques are applied to selected Raman bands to study the microscopic features of acetabular cups made of ultra-high molecular weight polyethylene (UHMWPE) before and after implantation *in vivo*. The micrometric lateral resolution of a laser beam focused on the polymeric surface (or subsurface) enables a highly resolved visualization of 2-D conformational population patterns, including crystalline, amorphous, orthorhombic phase fractions, and oxidation index. An optimized confocal probe configuration, aided by a computational deconvolution of the optical probe, allows minimization of the probe size along the *in-depth* direction and a nondestructive evaluation of microstructural properties along the material subsurface. Computational deconvolution is also attempted, based on an experimental assessment of the probe response function of the polyethylene Raman spectrum, according to a defocusing technique. A statistical set of high-resolution microstructural data are collected on a fully 3-D level on γ-ray irradiated UHMWPE acetabular cups both as-received from the maker and after retrieval from a human body. Microstructural properties reveal significant gradients along the immediate material subsurface and distinct differences are found due to the loading history *in vivo*, which cannot be revealed by conventional optical spectroscopy. The applicability of the confocal spectroscopic technique is valid beyond the particular retrieval cases examined in this study, and can be easily extended to evaluate *in-vitro* tested components or to quality control of new polyethylene brands. Confocal Raman spectroscopy may also contribute to rationalize the complex effects of γ-ray irradiation on the surface of medical grade UHMWPE for total joint replacement and, ultimately, to predict their actual lifetime *in vivo*. [DOI: 10.1117/1.2710247]

Keywords: ultra-high molecular weight polyethylene; confocal spectroscopy; hip joint; Raman spectrum.

Paper 05377RR received Dec. 28, 2005; revised manuscript received Jul. 31, 2006; accepted for publication Aug. 29, 2006; published online Mar. 5, 2007.

1 Introduction

While ultra-high molecular weight polyethylene (UHMWPE) remains one of the best polymeric materials for joint replacement, the most common cause of implant failure is the generation *in vivo* of polyethylene debris particles as a consequence of accelerated wear degradation.[1] These debris particles are treated as foreign substances by the body and eventually lead to osteolysis (bone resorption) and to the need for revision surgeries.[2] Many of the problems associated with

1083-3668/2007/12(1)/014011/14/$25.00 © 2007 SPIE

using UHMWPE in artificial joints can be traced back to the sterilization process of the polymer before implantation in the human body.[1,3] This decontamination process is typically accomplished by ^{60}Co γ-ray irradiation, whose main effect on the polyethylene microstructure is to generate free radicals through hemolytic bond cleavage. These free radicals can in turn lead to cross-linking and chain scission of the polymer, the dominance of one of these mechanisms over the other depending on the sterilization atmosphere. Cross-linking is dominant when γ-irradiation is made in nitrogen, while chain scission dominates for irradiation in air. Oxygen is extremely reactive with the free radicals produced by γ-irradiation and oxidation continuously uptakes in UHMWPE as the material ages.[4–6] Both scission and oxidation processes are especially important to the structural integrity of the polymer: (I) as the long chains are broken in the polymer structure, the resultant shorter chains are able to pack together more easily, leading to higher crystallinity and density; and (II) as the oxidative degradation proceeds, stiffening of the molecular chains occurs, which can lead to hardening but also to embrittlement of the polymeric structure. So far, specific trends in the microstructural development and related mechanical behavior of UHMWPE when changing the conditions for γ-ray irradiation have been somewhat empirically characterized and classified.[7,8] However, given the dramatic changes induced in the UHMWPE structure for slight differences in surface irradiation and their significant impact on both wear resistance and debris formation, a strict microstructural control is needed and new characterization methods are strongly required to help replace empirical optimizations of the polyethylene microstructure in favor of a more precise evaluation of relevant microscopic parameters.

This paper seeks to build up a fully nondestructive, high-resolution, 3-D spectroscopic tool for microstructural analysis of UHMWPE materials used in hip joint replacement. Given the peculiar nature of the spectroscopic problem, dealing with the characterization of the very surface neighborhood of the joint surface, and the high transparency of UHMWPE, conventional laser probes may fail to retrieve meaningful structural information. We propose here a new set of calibrations aimed at establishing the quantitative use of confocal Raman spectroscopic techniques to rationalize relevant microstructural parameters in the micrometric neighborhood of the surface of γ-irradiated UHMWPE acetabular cups and their complex evolution *in vivo*. The use of a confocal probe is shown to be particularly relevant in understanding the fine structure developed by γ-ray irradiation nearby the surface of the joint and surface deterioration. From a purely spectroscopic point of view, our efforts aim first at minimizing probe size in Raman assessments of UHMWPE and, thus the convolutive effects associated with its finite volume. Then, a confocal probe of optimized configuration is swept along the material subsurface to nondestructively detect with micrometric resolution microstructural gradients as a function of *in-depth* direction. Microstructural features in UHMWPE acetabular cups could be analyzed for the first time with micrometric resolution, and they reveal distinctly different patterns in the case of new joints (as-received from the maker) or joints retrieved after exposure *in vivo* for different durations.

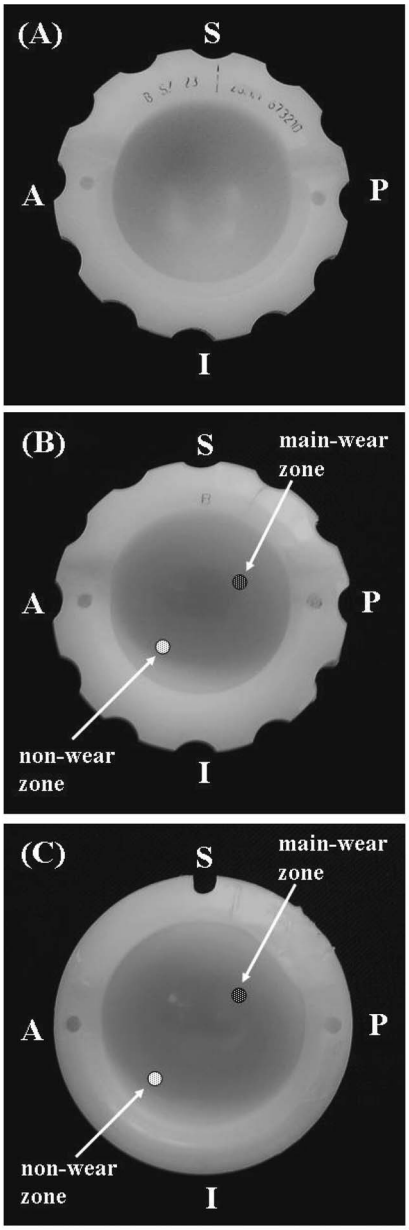

Fig. 1 Photographs of the investigated hip acetabular cups: (A) new cup; (B) short-term retrieved cup; and (C) long-term retrieved cup. The surface of each cup was irradiated by a γ-ray dose of 33 kGy.

2 Materials and Methods

2.1 *Materials*

One new [Fig. 1(A)] and two retrieved cross-linked UHMWPE acetabular cups [Figs. 1(B) and 1(C)] were investigated. The two retrieved acetabular cups were obtained at the time of revision surgery from total hip arthroplasty. All the acetabular components investigated in this study were manufactured by Biomet Japan Incorporated (Tokyo, Japan). New acetabular components (ArCom®, Biomet Incorporated) were made from GUR 1050 bar stock by isostatic compression molding (with no addition of calcium stearate) and successive surface irradiation by a γ-ray dose of 33 kGy. The manufacturing process adopted for the retrieved acetabular component shown in

Fig. 1(B) was the same as the previously described new components, except for the raw resin being of the 1900H type. The retrieved acetabular cup shown in Fig. 1(C) was made from GUR4150 bar stock by Ram extrusion molding (calcium stearate was added in this case); also, in this latter case, the surface irradiation γ-ray dose was 33 kGy. Of the two retrievals studied, one belonged to a 53-yr-old female patient for which the cause of revision was infection dislocation with a follow-up period of 2 yr 10 months (this cup, shown in Fig. 1(B), is simply referred to as "short-term retrieval"). The second retrieval also belonged to a female patient (60-yr-old) and the cause of revision was aseptic loosening after a follow-up period of 12 yr 2 months [in Fig. 1(C) and referred to as "long-term retrieval"]. The two retrievals were both from left hip joints, thus showing a main wear zone on the cup surface between the superior and the posterior poles [Figs. 1(B) and 1(C)]. On the other hand, a zone identified as a nonwear zone could be found on the surface portion between the inferior and the anterior poles of the cup.

2.2 *Raman Spectroscopic Assessments*

Raman spectra were collected with a triple monochromator spectrometer (T-64000, ISA Jovin-Ivon/Horiba Group, Tokyo, Japan) equipped with a charge-coupled detector (high-resolution CCD camera). The laser power on the UHMWPE surface was typically about 70 mW at the laser head. The laser excitation source was a monochromatic blue line emitted by an Ar-ion laser at a wavelength of 488 nm. The spectral integration time was typically 20 s, and the recorded spectra were averaged over three successive measurements at each selected location. All Raman spectra were recorded at room temperature. The wavenumbers of Raman band maxima were retrieved by fitting the CCD raw data to mixed Gaussian/Lorentzian curves with commercially available software (Labspec, Horiba Company, Kyoto, Japan). UHMWPE acetabular cups were placed on an automatic mapping device (with lateral resolution of 0.1 μm), which was connected to a personal computer to drive highly precise displacements (along both x and y axes) on the sample. Given the curved nature of the investigated surfaces, an autofocus device was used throughout the automatic mapping experiments to sharpen the optical probe at selected surface or subsurface locations. Confocal experiments were conducted with focusing the waist of the laser beam from the surface toward subsurface planes of the joint through an optical lens ($\times$100). The Raman scattered light was then refocused onto a small confocal aperture (pinhole) that acted as a spatial filter, passing the signal excited at the beam waist, but substantially eliminating the Raman emission from volume portions above and below the beam focal plane. The filtered signal was then returned to the spectrometer (via the same optical lens used to focus the incoming laser), where it was dispersed onto a CCD camera to produce a Raman spectrum. A pinhole aperture was placed in the optical train of the spectrometer and used to regulate the rejection of light from regions outside the focal plane (confocal spectroscopy). Selected xyz locations in the samples were probed nondestructively with micron (lateral) spatial resolution according to the following procedure: 2-D data maps were first built up by scanning surfaces parallel to the free surface of the sample (xy scanning); then, 3-D distributions were produced by sequentially acquiring data on xy slices from different *in-depth* planes (along the z axis perpendicular to the free surface of the sample). Figure 2 shows a schematic of the confocal probe when shifted along the sample subsurface at positions (x_0, y_0, z_0).

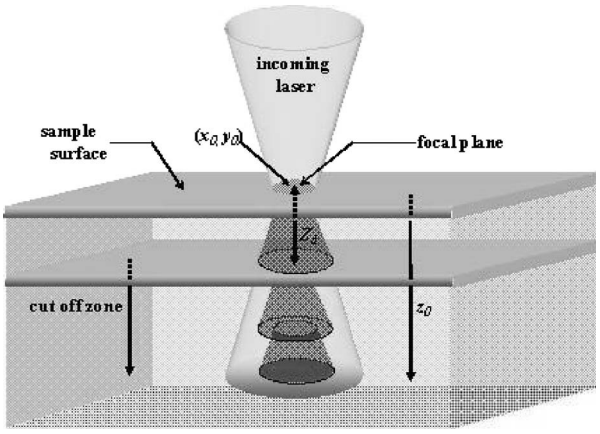

Fig. 2 Schematics of the optical probe configuration and related parameters.

3 Theoretical Background

3.1 *Vibrational Modes and Microstructure of Polyethylene*

The relationship between the observed Raman bands and the vibrational modes of the polyethylene molecular structure has been amply documented in the literature.[9,10] However, we briefly repropose hereafter the salient features of the Raman spectrum that are pertinent to the remainder of this work. A typical Raman spectrum of UHMWPE is shown in Fig. 3(A). This spectrum (taken in the range between 1000 and 1600 cm^{-1}) can be divided into three main subregions: region (I) at 1000 to 1150 cm^{-1} is dominated by the C-C stretching vibration mode; region (II) is mainly represented by the $-CH_2-$ twisting vibration at around 1300 cm^{-1}; and region

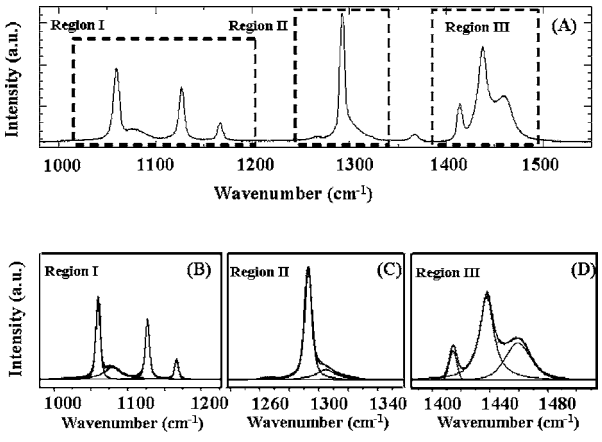

Fig. 3 (A) Typical Raman spectrum of UHMWPE as collected in an acetabular cup; (B), (C), and (D) represent the fitting deconvolution of bands collected in the three different regions of the spectrum defined in (A).

(III) is characteristic of -CH_2- bond wagging between 1350 and 1500 cm^{-1}. Figures 3(B)–3(D) represent the results of a fitting procedure applied to regions (I), (II), and (III) of the polyethylene spectrum [broken lines in Fig. 3(A)]. The broad band located at 1080 cm^{-1} is associated with the presence of an amorphous phase. The peak at 1414 cm^{-1} is characteristic of an orthorhombic crystalline phase, while the intensity of the peak located at 1293 cm^{-1} can be used to approximate the overall degree of crystallinity of the UWMWPE structure.[9,10] Note that specific vibrational modes are not directly related to long-range 3-D order, but they are related to conformational state populations, which may lead to 3-D crystallinity. Therefore, when a crystallinity fraction is mentioned in the remainder of this work, it refers to conformational populations that are present in both crystalline and noncrystalline regions of the material. These features of the Raman spectrum make it possible to quantitatively analyze the volume fraction of orthorhombic (α_o), amorphous (α_a), and crystalline (α_c) phases by calculating them from the relative intensities of selected Raman bands of UHMWPE, according to the following equations:

$$\alpha_o = \frac{I_{1414}}{0.46(I_{1293} + I_{1305})}, \tag{1}$$

$$\alpha_a = \frac{I_{1080}}{0.79(I_{1293} + I_{1305})}, \tag{2}$$

$$\alpha_c = \frac{I_{1293}}{(I_{1293} + I_{1305})}, \tag{3}$$

where I is the integral intensity of the Raman band whose wavenumber is identified by the subscript. The fraction of the matter in an anisotropic (intermediate) disordered state (usually referred to as the "third phase"[11]) α_b can then be expressed as follows:

$$\alpha_b = 1 - (\alpha_c + \alpha_a). \tag{4}$$

The previous equations constitute the basis of the Raman spectroscopic method for characterizing a partially crystalline structure in UHMWPE.

The extent of overall oxidation and specifically certain oxidation index profiles present in orthopaedic implant components made of UHMWPE have been shown to degrade their mechanical properties and thus potentially adversely affect their *in-vivo* performance.[12] In order to measure the amount of oxidation in UHMWPE, an oxidation index (OI) has been defined.[13] The OI index can be measured by Fourier transformed infrared (FTIR) spectroscopy by monitoring the ratio of the area of absorption peaks between 1650 and 1850 cm^{-1} to the area of absorption peaks between 1330 and 1396 cm^{-1}. Raman spectroscopy has also been used for investigating the oxidation degree of UHMWPE. Chenery[14] identified the marker bands of oxidation products at 870 cm^{-1} (peroxy), 935 cm^{-1} (epoxy), 1151 cm^{-1} (alcohol), 1770 cm^{-1} (peroxy acid), and 1794 cm^{-1} (acyl peroxy). However, Raman spectroscopic assessments based these bands have proved unable to detect low levels of oxidation in UHMWPE.[15] We performed both Raman and infrared spectroscopy characterizations on a series of UHMWPE oxidized samples[16] and came across a phenomenological relationship between OI and α_o for UHMWPE, as follows:

$$\alpha_o = 0.56 + 0.15 \arctan\left(\frac{\ln OI + 0.13}{1.19}\right). \tag{5}$$

Rearranging Eqs. (1) and (5), we obtain:

$$\mathrm{OI} = \exp\left\{1.19 \times \tan\left[14.26\left(\frac{I_{1414}}{I_{1293} + I_{1305}} - 0.26\right)\right] - 0.13\right\}. \tag{6}$$

Explanations about the procedure for determining Eq. (6), a brief discussion, and details on the reliability of the present Raman measurements are given in the Appendix in Sec. 6. While Eq. (6) was obtained on "controlled" experiments in which a virgin and unstressed polyethylene cup was held for increasing times in an O_2 atmosphere (for testing conditions, see the Appendix in Sec. 6), it should be also noted that many changes may occur in polyolefins in service. Stress/strain-induced crystallization can be very significant,[17] and oxidative attack can form shorter chains terminated in acid carbonyls or ester carbonyls or ketones along backbone.[18] Interestingly, we could not find a precise relationship between the overall degree of crystallinity α_c and OI; we only found it between the orthorhombic phase fraction α_o and OI. Clearly, it is difficult at this time to generalize Eq. (6) by extrapolating results obtained *in vitro* to any service condition for UHMWPE. On the one hand, we show here that Eq. (6) can be used to a degree of precision for OI assessments (and that this practice is useful because it enables the determination of OI nondestructively from the same spectral records used for analyzing microstructural features in polyethylene). On the other hand, given the possible lack of generality of Eq. (6), the OI values measured here should be more generally regarded as "wear index" (WI) values, in which the observed crystallinity changes may not only be those directly due to oxidation but also those simply occurring in concomitance with oxidation. Despite this, a comparative increase in WI value should definitely represent the degree of surface or subsurface degradation of a UHMWPE cup in service.

3.2 *Probe Response Function*

The observed intensity of the Raman spectrum depends on the intensity distribution of scattered light around the irradiation point (x_0, y_0, z_0). This intensity distribution is called the *probe response function* $B(x, y, z, x_0, y_0, z_0)$, and represents the intensity of the light scattered from a given point (x, y, z) when the incident beam is focused at the point (x_0, y_0, z_0):[19,20]

$$B(x,y,z,x_0,y_0,z_0) \propto \exp\left[-\frac{(x-x_0)^2 + (y-y_0)^2}{2R^2}\right] \times \frac{p^2}{(z-z_0)^2 + p^2} \exp(-2\alpha z), \tag{7}$$

where $2R$ is the laser beam diameter in the focal plane, p is the *probe response parameter* (for an unfocused beam, p tends to infinity), and α is the absorption coefficient of the material at the incident wavelength. For Raman bands, the

term 2α in Eq. (7) may need to be substituted by the sum of the absorption coefficients for incident and emitted light. If the variation of all the variables in the *xy* plane can be ignored, the probe response function can be greatly simplified as follows:

$$B(z,z_0) \propto \exp(-2\alpha z)\frac{p^2}{p^2+(z-z_0)^2}. \tag{8}$$

The observed spectral intensity at band maximum can be then obtained according to a simple volumetric integration:

$$I_{obs}(\omega_p) \propto \int_{-\infty}^{\infty} \exp(-2\alpha z)\frac{p^2}{p^2+(z-z_0)^2}dz, \tag{9}$$

where ω_p is the wavenumber at the maximum of the selected spectral band. The focal plane position (above or below the sample surface) z_0 can also be seen as a defocusing distance with respect to a laser irradiation with the focal plane placed on the sample surface. The maximum intensity $I_{\max} \cong I_{surf}$ of a selected band of the spectrum when varying defocusing distance z_0 can be used to normalize the band intensity, thus translating Eq. (9) into a fully quantitative equation for band intensity assessment:

$$\frac{I_{obs}(\omega_p)}{I_{\max}(\omega_p)} = \frac{\int_0^{\infty} \exp(-2\alpha z)\frac{p^2}{p^2+(z-z_0)^2}dz}{2\int_0^{\infty} \exp(-2\alpha z)\frac{p^2}{p^2+z^2}dz}. \tag{10}$$

Note that no analytical integration is generally possible for this equation, which has to be integrated numerically. As the probe is swept along the *in-depth* axis, the collected intensity function $I_{obs}(\omega_p)$ maps the probe response. The probe response parameter p and the absorption coefficient α can then be obtained from the best fitting of the (normalized) experimental intensities to the calculated ones [according to Eq. (10)]. The prior method for determining the probe function through shifting the focal plane can be referred to as the "defocus method." To visualize the probe size in terms of penetration depth, a probe depth z_d can be defined according to the following equation (using 90% of the maximum intensity as a threshold value for intensity distribution):

$$\frac{\int_0^{z_d} \exp(-2\alpha z)B(z,z_0)dz}{\int_0^{\infty} \exp(-2\alpha z)B(z,z_0)dz} = 0.9. \tag{11}$$

Also, this equation can be solved numerically. Most of the equations used in this work were solved with the aid of a commercially available computational software package (Mathematica, Wolfram Research, Incorporated). The *in-depth* resolution of the Raman probe can be improved by placing a confocal pinhole at the back-focal image plane to partly cut off the light scattered from outside the laser focal area. By employing this technique, referred to as confocal spectroscopy, it is possible to probe discrete z planes with relatively high *in-depth* spatial resolution. When the laser is focused on the specimen surface ($z_0=0$), there exists an inner transmitted zone for the scattered/emitted light within a solid angle $\theta \leq \theta_{tr}$, varying as a function of the depth position z. The collection solid angle Ω, which takes into account the competitive effects of the numerical aperture of the objective lens (NA) and of the pinhole aperture, can be expressed as follows:

$$\Omega = 2\pi(1-\theta_{tr}) = \begin{cases} 2\pi\left(1-\dfrac{z}{\sqrt{z^2+\rho_0^2}}\right) & (\rho_{\max} \geq \rho_0) \\ 2\pi\left(1-\dfrac{z}{\sqrt{z^2+\rho_{\max}^2}}\right) & (\rho_{\max} \leq \rho_0) \end{cases}, \tag{12}$$

$$z = \rho_{\max}\left[(n^2-1)+\left(\frac{f}{D/2-\rho_{\max}}\right)^2 n^2\right]^{1/2}, \tag{13}$$

where $\rho_{\max}$ is the maximum transverse ray aberration from the optical axis (determined by the NA of the objective lens); the confocal pinhole with diameter Φ has a virtual back image $2\rho_0$ in the sample focal plane given by the relation $\Phi = 2\rho_0 MPG$, where MP is the magnification power of the objective and G is the enlargement factor (1.4); note that only lights from within the virtual circle $2\rho_0$ on the surface can pass through the pinhole; n is the refractive index of the material; and D/f is the diameter/focal length of the objective lens. For any given z value, $\rho_{\max}$ can be derived from Eq. (13). The collection solid angle remains almost invariant near the surface; then, it falls pronouncedly because of the filtering effect of the confocal pinhole aperture. The smaller the pinhole aperture, the more abrupt the Ω drops. By reducing the diameter of the pinhole aperture Φ, the critical subsurface depth z, at which the Ω value significantly drops, gradually approaches the sample surface. In principle, probe depth can be reduced down to the laser wavelength by reducing the diameter of the pinhole aperture. However, a significant drop in the efficiency of the collected spectrum with reducing Φ greatly limits the achievable *in-depth* resolution. In the experimental practice, problems related to the acquisition time for polyethylene Raman bands involve minimum pinhole apertures to be selected in the range $20 \leq \Phi \leq 100$ μm. The observed spectrum is thus obtained by combining all the spectra originating from different points within the volume of the probe in the confocal configuration:

$$I_{\text{obs}}(\omega_p) \propto \int_0^{\infty} I_{(\omega)}\Omega(z,z_0,\rho_0)\frac{p^2}{p^2+(z-z_0)^2}\exp(-2\alpha z)dz, \tag{14}$$

where $I_{(\omega)}$ is the local Raman line shape. When the focal plane is placed on the sample surface, Eq. (14) can be rearranged to give the observed intensity I_{obs} as follows:

$$I_{obs}(\omega_p) \propto \int_0^t \Omega(\rho_{\max} \leq \rho_0)\exp(-2\alpha z)\frac{p^2}{z^2+p^2}dz + \int_t^\infty \Omega(\rho_{\max} \geq \rho_0)\exp(-2\alpha z)\frac{p^2}{z^2+p^2}dz, \tag{15}$$

where t is a threshold value of the *in-depth* abscissa, below which the collection solid angle abruptly drops down:

$$t = \rho_0\left[(n^2-1)+\left(\frac{f}{D/2-\rho_0}\right)^2 n^2\right]^{1/2}. \tag{16}$$

Equation (15) can be eventually normalized to the maximum spectral intensity, as done for Eq. (10). When the confocal pinhole is set to a given aperture and the focal plane is placed on the sample surface ($z_0=0$), we can calculate the probe depth z_d by solving the following equation:

$$\frac{\int_0^{z_d} S(z,\rho_0)B(z)dz}{\int_0^{\infty} S(z,\rho_0)B(z)dz} = 0.9, \tag{17}$$

where the collection cross section, $S(z,\rho_0)$, is given by:

$$S(z,\rho_0) = \Omega(z,\rho_0,\rho_{\max})\exp(-2\alpha z). \tag{18}$$

Note that in nonhomogeneous materials, the absorption coefficient α should be replaced with the effective absorption coefficient α_{eff}, which takes into account inhomogeneous light scattering.

In the case of a small pinhole aperture ($\rho_0 \to 0$), the collection solid angle can be approximated by the following function [Eq. (12)]:

$$\Omega(z,z_0,\rho_0 \approx 0) = A + \frac{B}{C+(z-z_0)^2}. \tag{19}$$

On defining p_c as the apparent probe response parameter retrieved from best fitting the defocusing results in the confocal configuration, Eq. (19) can be rewritten as a function of p_c and p, namely the probe response parameter characteristic of a probe configuration with full pinhole aperture (also referred to as normal probe configuration). Accordingly, $\Omega(z,z_0)$ can be expressed by:

$$\Omega(z,z_0) = \frac{p_c^2}{p^2}\left[1+\frac{p^2-p_c^2}{p_c^2+(z-z_0)^2}\right]. \tag{20}$$

It should be pointed out that the previous equation represents an approximation of the exact expression of the solid collection angle and it is only valid at small pinhole apertures. In addition, p_c is just a numerical parameter function of the probe configuration, thus losing its physical meaning as a material property (*i.e.*, as in the case of p). Equations (10) and (15) can be used to precisely determine the relevant optical parameters and material properties through a best-fitting iterative routine of experimental data. In addition, Eqs. (11) and (17) can be used to assess the probe geometry (in particular, the probe depth) of confocal and nonconfocal probes in UHMWPE. These procedures are shown in details in the next section.

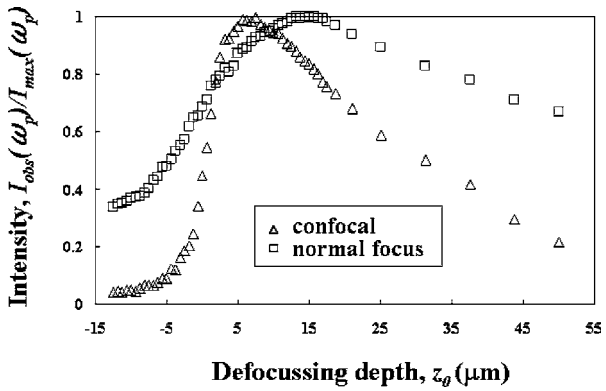

Fig. 4 Normalized plot of probe response functions (*i.e.,* Raman band intensity $I_{obs}(\omega_p)/I_{\max}(\omega_p)$ for UHMWPE as a function of defocusing depth z_0) for normal and confocal probe configurations.

4 Results and Discussion

4.1 *Quantitative Assessment of Confocal Probe Geometry in Ultra-High Molecular Weight Polyethylene*

The intensity of the Raman lines of UHMWPE was collected as a function of defocus displacement z_0 along the *in-depth* direction perpendicular to the sample surface both in the normal probe and in the confocal probe configuration ($\Phi = 100\ \mu$m). A complete coincidence was observed in the optical behavior of bands belonging to the same phase. Therefore, no specification is henceforth given in the discussion of the probe response function about the wavenumber at the maximum of the selected band. The experimental (normalized) intensity trends (*i.e.*, the probe response functions) are shown in Fig. 4 for both normal and confocal probe configurations. No detectable difference was found for probe response functions recorded on new and retrieved cups for each respective probe configuration. However, from data shown in Fig. 4, it can be seen that a significant difference exists in the defocusing behavior of UHMWPE when the probe configuration is altered. The optical parameters, by which the best fitting of the probe response function was obtained, were determined by solving Eqs. (10) and (15) for normal and confocal ($\times 100$ objective lens, NA=0.9, $\Phi = 100\ \mu$m, and $f = 0.3$ mm) probe configurations, respectively. The results of this fitting procedure are shown in Table 1, together with the probe depth z_d calculated according to Eqs. (11) and (17) for normal and confocal probe configurations, respectively. As is seen, the p_c value found for the confocal configuration was about five times smaller than the p value found for the through-focus configuration. This behavior is reflected in a significantly shallower probe penetration depth in confocal than in normal probe configuration. No significant difference was found between calculations based on data of peak intensity at maximum and integral band intensity. One important implication in comparing the findings of these calibration procedures is that spectra collected by nonconfocal probe con-

Table 1 Probe characteristics in both confocal and normal configurations as determined in different UHMWPE samples. Parameters are compared when determined from spectral band intensity and from integral band intensity.

		Confocal probe		Normal probe	
		Intensity	Integral intensity	Intensity	Integral intensity
New	$\alpha\ (m^{-1})$	0.04	0.04	0.009	0.011
	$p, p_c\ (\mu m)$	2.4	2.5	12	12
	$z_d\ (\mu m)$	6.4	6.5	30.3	27.9
Short term	$\alpha\ (m^{-1})$	0.02	0.02	0.01	0.01
	$p, p_c\ (\mu m)$	2.4	2.6	12	12
	$z_d\ (\mu m)$	8.1	8.5	29.1	29.1
Long term	$\alpha\ (m^{-1})$	0.01	0.018	0.01	0.01
	$p, p_c\ (\mu m)$	2.5	2.5	14.1	12.9
	$z_d\ (\mu m)$	10	8.6	31.9	30.4

figuration may average spectral information from significantly larger portions of subsurface as compared to a confocal probe configuration. Accordingly, the differences in the measured microstructural features can be very pronounced, especially in the presence of large and steep property gradients along the sample subsurface. In this context, the use of a confocal probe configuration seems to be mandatory for polyethylene components to correctly interpret spatially resolved Raman spectroscopic data. Nevertheless, although the probe penetration depth can be reduced to values $z_d \approx 6.4 \div 10\ \mu$m by using a confocal probe ($\Phi = 100\ \mu$m), further minimization of convolutive effects on the measured property gradients may be required, which can only be performed according to a mathematical deconvolution procedure based on the knowledge of the probe response function $B(z, z_0)$ (see Sec. 4.3).

4.2 *Three-Dimensional Microstructural Distributions in Ultra-High Molecular Weight Polyethylene Acetabular Cups*

For characterizing microstructural patterns along the material subsurface, Raman spectroscopic analyses were first performed on a new acetabular cup and then, for comparison, on both nonwear and main wear zones of retrieved acetabular cups. The confocal configuration of the probe, as optimized in the previous section ($\times 100$ objective lens, NA$=0.9$, $\Phi = 100\ \mu$m, and $f = 0.3$ mm), was employed throughout the characterization. Figures 5(A)–5(E) show maps of crystalline phase volume fractions collected at increasing laser penetration depths on the new UHMWPE acetabular cup [shown in Fig. 1(A)]. Figures 6(A)–6(E) and 6(F)–6(J) are similar maps collected on the nonwear and main wear zones, respectively, of the short-term retrieval shown in Fig. 1(B). Figures 7(A)–7(E) and 7(F)–7(J) represent maps of crystalline volume fractions collected on the nonwear and main wear zones of the acetabular cup retrieved after long-term implantation, which is shown in Fig. 1(C). When the confocal probe was shifted from the surface toward the subsurface of the new acetabular cup, only a slight increase was noticed in the crystalline phase fraction. A similar trend but with slightly larger values of crystallinity was found for both nonwear and main wear zones of the acetabular cup retrieved after short-term exposure *in vivo*. This phenomenon can be partly explained due to a layer of UHMWPE removed from the cup surface. However, this explanation does not apply to the nonwear zone, in which no abrasive effect is expected. Therefore, we propose that the increase in crystallinity uniformly observed on the cup surface may partly arise from an *in-vivo* oxidation process, taking place even within a short-term implantation. On the other hand, a significant increase in crystalline volume fraction was observed when the Raman probe was shifted from the surface toward the subsurface of the long-term retrieval. In particular, a high increase in α_c values was found at depths $\geq 15\ \mu$m, especially in the main wear zone. It is clear from these data that both a longer exposure *in vivo* and the effect of wear can significantly alter both the amount of crystallinity in the UHMWPE structure and its subsurface gradient. Increase in crystallinity near the surface of the cup has been reported to be due to the recrystallization of chains scissioned by irradiation.[21–23] In addition, after long-term implantation, UHMWPE hip cups were shown to develop a subsurface zone of increased density and crystallinity, about 1 mm below the sample surface.[24] This has been explained as a "stress effect."[25] In this study, we show that a steep gradient in crystallinity, which is clearly of different origin as compared to the previous one, is also present in the immediate subsurface of acetabular cups exposed for relatively long times *in vivo*. Such a steep gradient can be visualized only by using a confocal probe (this point is better clarified in the next section). This increase in crystallinity with increasing storage time *in vivo* may arise from an increased scission associated with oxidation. The initial stage of this process has indeed been observed in the short-term retrieval. In this context, diffusion of

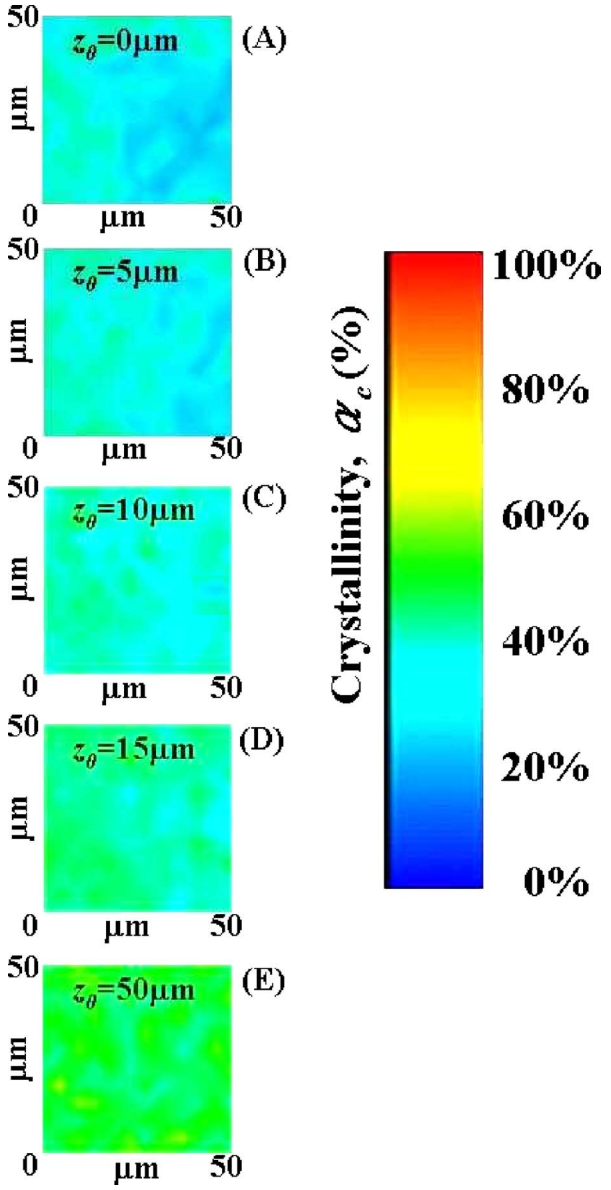

Fig. 5 Maps of crystalline phase volume fractions collected at increasing depths of focal plane z_0 of the confocal probe on the new UHMWPE acetabular cup shown in Fig. 1(A).

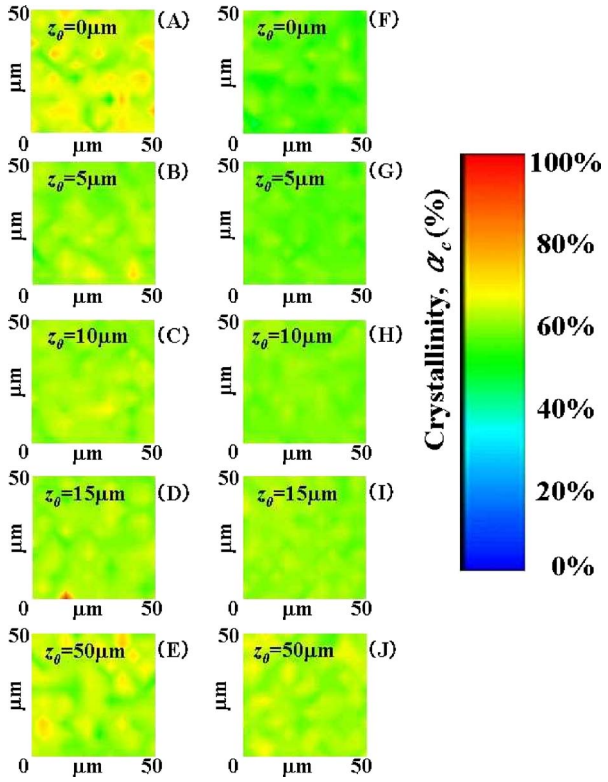

Fig. 6 Maps of crystalline phase volume fractions collected at increasing depths of focal plane z_0 of the confocal probe on the short-term retrieved UHMWPE acetabular cup shown in Fig. 1(B): (A) through (E) refer to the nonwear zone, while (F) through (J) refer to the main wear zone of the retrieved cup.

oxygen along the subsurface, eventually assisted by local contact strain fields, occurs up to a saturation point (characteristic of each depth) and is the rate-controlling phenomenon for crystallization, as confirmed by the clear relationship found between α_o and the oxidation index of the material.[16] Figures 8(A)–8(E) show 2-D maps of oxidation index as a function of probe penetration depth along the subsurface of a new cup. As is seen, there is no gradient of oxidation along the immediate subsurface of the as-received acetabular cup, while a small amount of oxidation was observed in the short-term implanted retrieval, both in the nonwear and in the main wear zones [Figs. 9(A)–9(E)and 9(F)–9(J), respectively]. On the other hand, significant oxidation gradients were found along the subsurface of the long-term implanted retrieval, as shown in Figs. 10(A)–10(J), especially in the main wear zone. Note that a clear relationship is found between orthorhombic crystalline fraction and degree of oxidation along the subsurface, and this can be explained with the occurrence of partial crystallization of the polyethylene structure on oxidation. In this context, it is important to note that our confocal experiments here show a region of relatively high crystallinity as developed in the immediate subsurface of the cup during implantation lifetime *in vivo*. The formation of this region may be directly related to the formation of polyethylene debris on wear contact. In other words, the near-surface microstructure of UHMWPE is further crystallizing (and oxidizing) with aging *in vivo*, which may induce significant embrittlement of the polymeric subsurface structure due to oxidative chain scission.

4.3 *Mathematical Deconvolution in the Confocal Probe Volume*

Linear profiles (each data point was averaged among 2500 measurement points) are shown in Figs. 11, 12, and 13 for average values of crystalline, amorphous, orthorhombic, and third phases, while Fig. 14 shows linear profiles of subsurface oxidation (more precisely, of subsurface wear index *WI*, as discussed in Sec. 3.1) in new, short-term, and long-term implanted acetabular cups, respectively. These profiles, retrieved in the main wear zones of both the retrieved cups, were obtained according to Eqs. (1)–(5) applied to spectra collected with the optimized confocal probe, and thus, with an *in-depth* resolution of $z_d \approx 6.4 \div 10$ μm. These figures summarize the average fraction values shown in the maps of Figs. 5–10.

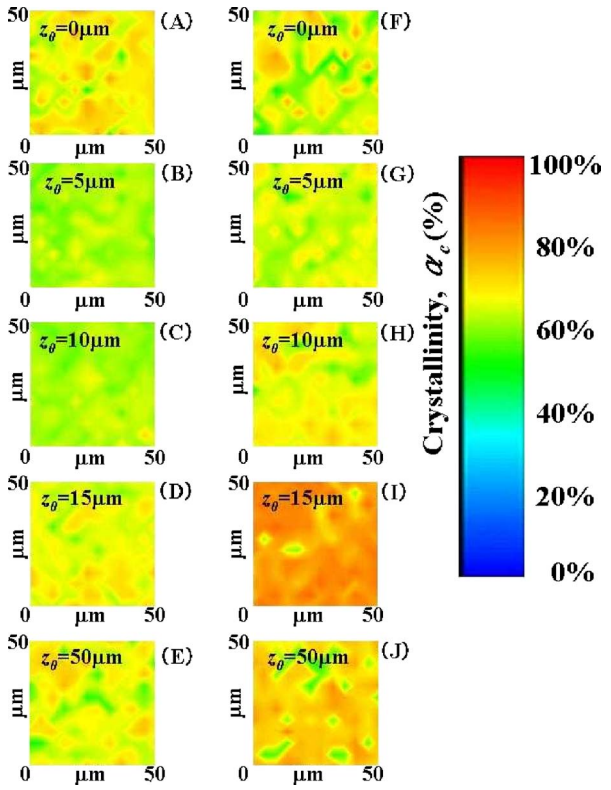

Fig. 7 Maps of crystalline phase volume fractions collected at increasing depths of focal plane z_0 of the confocal probe on the long-term retrieved UHMWPE acetabular cup shown in Fig. 1(C): (A) through (E) refer to the nonwear zone, while (F) through (J) refer to the main wear zone of the retrieved cup.

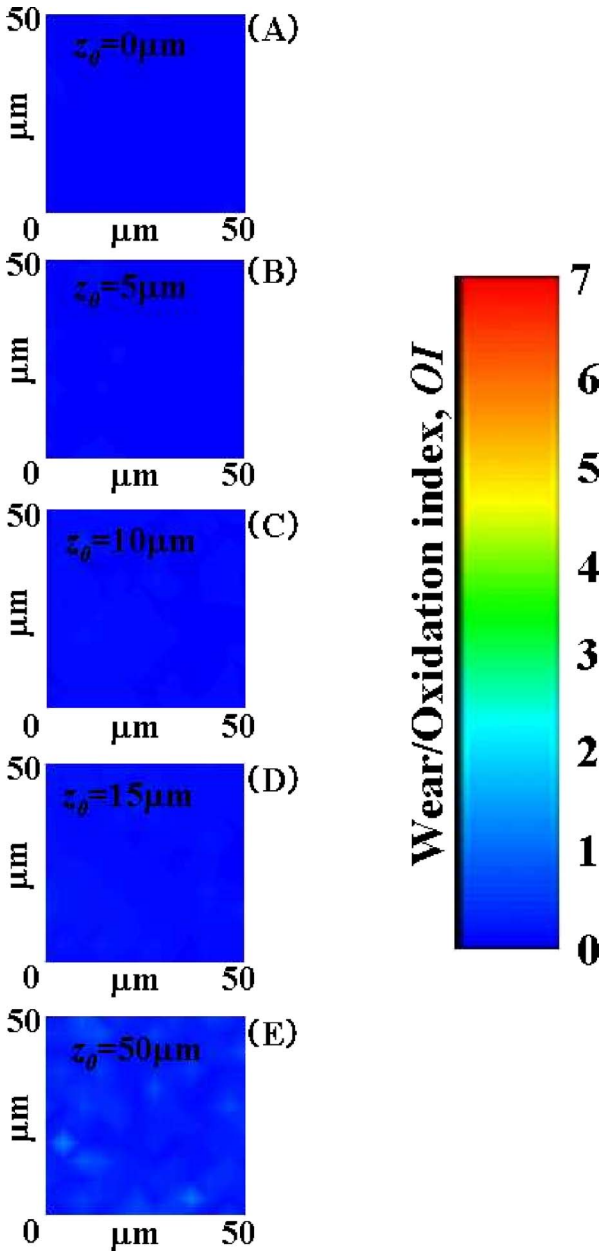

Fig. 8 Maps of wear index (related to oxidation index) collected at increasing depths of focal plane z_0 of the confocal probe on the new UHMWPE acetabular cup shown in Fig. 1(A).

While no significant variation in properties was found for the new cup as a function of the *in-depth* abscissa z, property gradients were clearly observed in the material subsurface of retrievals, especially for the long-term retrieved acetabular cup. It should be noted that, from a purely mathematical point of view, the invariance of properties observed in the new cup does not necessarily imply that a property gradient is absent along the subsurface; however, given the rather small size of our probe, it seems plausible to assume that the observed property function of *in-depth* abscissa is still representative of the actual subsurface distribution, though convoluted by the finite size of the probe. In other words, the detected gradient for a given property along the *in-depth* abscissa may be significantly less steep than the actual gradient due to probe convolution, even when adopting a confocal probe configuration. According to the knowledge of the response function of the laser probe, the convoluted property value $\overline{\alpha_p}$ detected by a confocal probe can be expressed as follows:

$$\overline{\alpha_p} = \frac{\int_0^\infty \alpha_p(z)\Omega(z,z_0,\rho_0)\exp(-2\alpha z)\dfrac{p^2}{(z-z_0)^2+p^2}dz}{\int_0^\infty \Omega(z,z_0,\rho_0)\exp(-2\alpha z)\dfrac{p^2}{(z-z_0)^2+p^2}dz}, \tag{21}$$

where this equation has to be set for each focal position z_0. Note that, from a purely mathematical point of view, Eq. (21) cannot be solved for $\alpha_p(z)$ unless the character of this function is known. In other words, a hint is needed about the actual physical nature of the subsurface property profile.

Premnath et al.[26] proposed a theory to explain the mechanisms of subsurface oxidation in UHMWPE as a consequence of surface irradiation. According to this model, γ-irradiation induces the formation of free radicals, predominantly alkyl but also allyl and peroxyl groups, while oxidation is detected as the production of carbonyls (mainly ketons) produced in the reaction between alkyl and peroxyl radicals. Therefore, it is from the balance between the alkyl and peroxyl radical fractions formed during irradiation that an oxidation profile is formed along the material subsurface. In polyethylene mate-

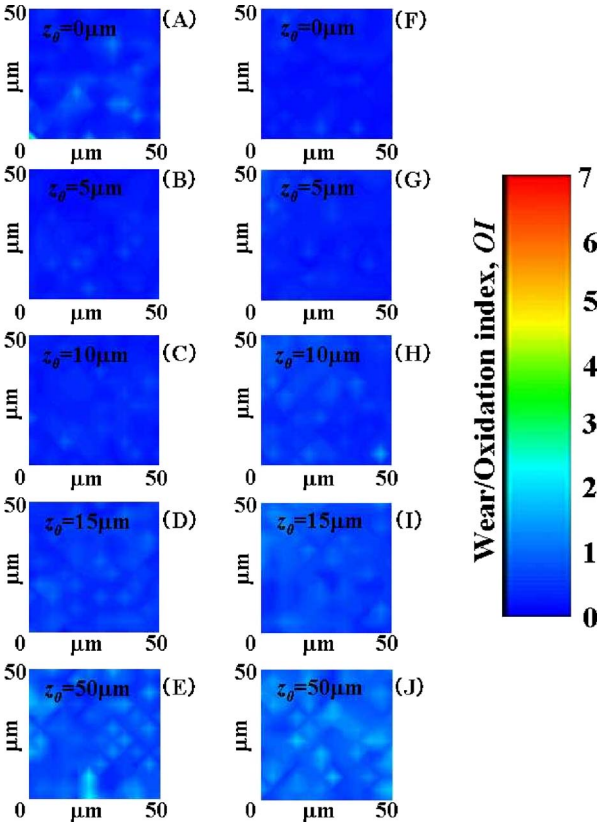

Fig. 9 Maps of wear index (related to oxidation index) collected at increasing depths of focal plane z_0 of the confocal probe on the short-term retrieved UHMWPE acetabular cup shown in Fig. 1(B): (A) through (E) refer to the nonwear zone, while (F) through (J) refer to the main wear zone of the retrieved cup.

rials irradiated in a controlled atmosphere, oxidation during irradiation is negligible and the majority of the generated free radicals lead to cross-linking; however, chain scission may partly take place *in vivo* after irradiation and give rise to a time-dependent evolution of the oxidation profile, as observed in this study. During *in-vivo* exposure of the acetabular cup, the large availability of oxygen on the surface creates excess of peroxyl versus depletion of alkyl radicals. On the other hand, in bulk, oxygen levels are low, as it is the conversion of alkyl to peroxyl radicals, leading to an excess of alkyl over peroxyl radicals. At some depth below the surface, the fractions of alkyl and peroxyl radicals balance and the probability of a reaction to form ketons reaches a maximum, coincident with the observed maximum of oxidation. In other words, the physics behind the formation of an oxidation profile in the immediate subsurface of irradiated polyethylene dictates that the profile be rather of a sigmoidal shape than a continuously rising (*e.g.*, logarithmic or exponential) curve. Accordingly, we selected a trial function of the following type to perform a property deconvolution according to Eq. (21):

$$\alpha_p(z) = a + b \cdot \arctan(cz + d). \tag{22}$$

Note that oxidation results in substantial chain scission, accompanied by significant decrease in cross-linking and easier formation of thin crystallites in the amorphous regions as a consequence of chain rearrangement. Since the described oxidation process and the degree of crystallization are intrinsically related, we assumed, in the first approximation, the same trial function for probe deconvolution of both profiles. The crystallinity fraction $\alpha_c(z)$ and the oxidation index $OI(z)$ in the long-term retrieved cup were retrieved (and plotted in Figs. 15 and 16, respectively) as a function of the *in-depth*

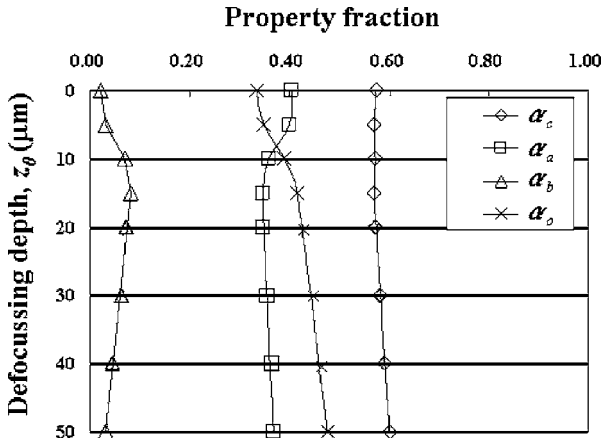

Fig. 11 *In-depth* profiles of crystalline, amorphous, orthorhombic, and third phases in the new acetabular cup. Probe resolution in this assessment was in the range $z_d \approx 6.4 \div 10$ μm.

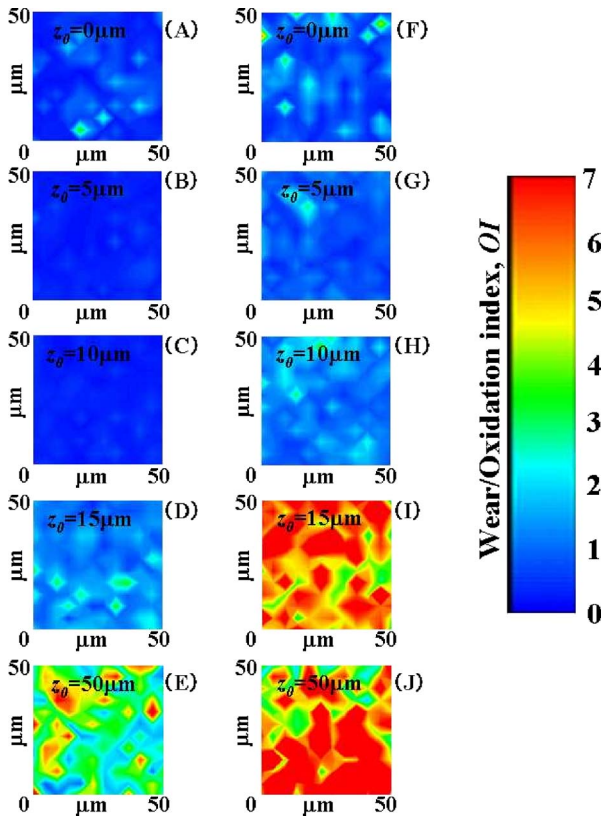

Fig. 10 Maps of wear index (related to oxidation index) collected at increasing depths of focal plane z_0 of the confocal probe on the long-term retrieved UHMWPE acetabular cup shown in Fig. 1(C): (A) through (E) refer to the nonwear zone, while (F) through (J) refer to the main wear zone of the retrieved cup.

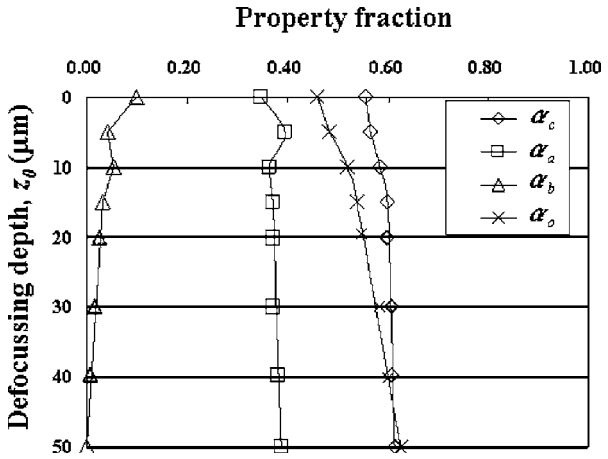

Fig. 12 *In-depth* profiles of crystalline, amorphous, orthorhombic, and third phases in the short-term retrieved acetabular cup. Probe resolution in this assessment was in the range $z_d \approx 6.4 \div 10$ μm.

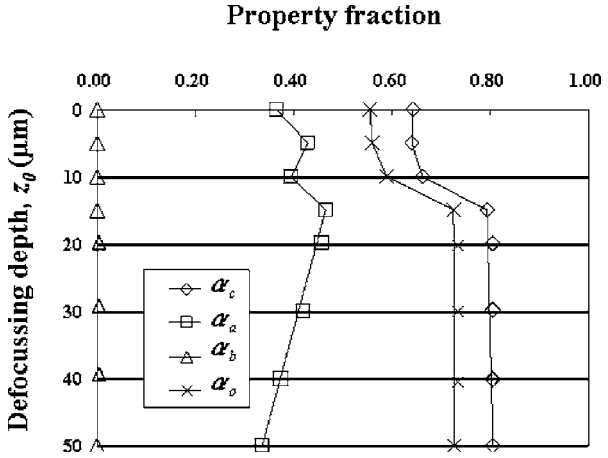

Fig. 13 *In-depth* profiles of crystalline, amorphous, orthorhombic, and third phases in the long-term retrieved acetabular cup. Probe resolution in this assessment was in the range $z_d \approx 6.4 \div 10$ μm.

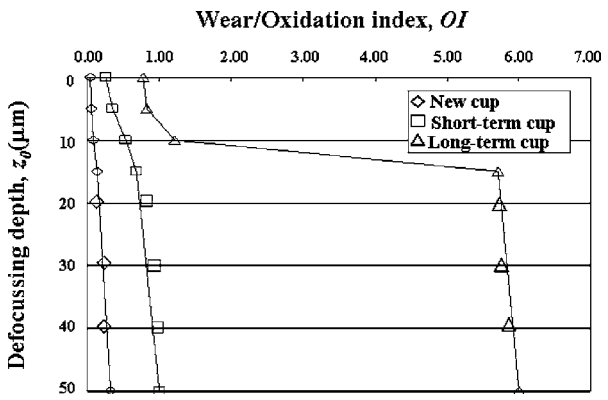

Fig. 14 *In-depth* profiles of wear/oxidation index in new, short-term, and long-term retrieved acetabular cups. Probe resolution in this assessment was in the range $z_d \approx 6.4 \div 10$ μm.

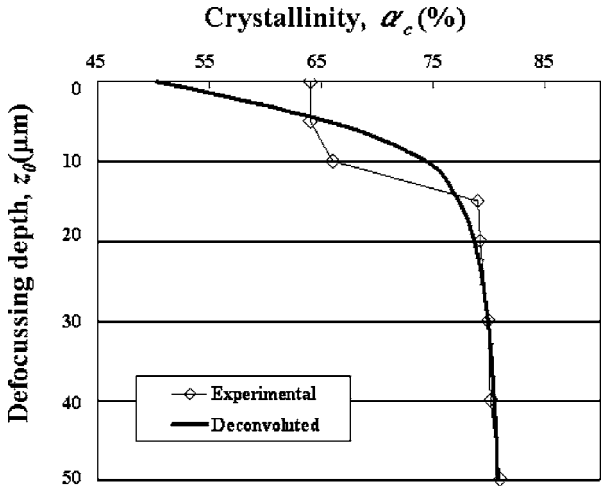

Fig. 15 Plots of crystallinity phase fraction distribution along the *in-depth z* axis as experimentally detected by the confocal probe and after mathematical probe deconvolution according to Eq. (20). In the calculation, Eq. (21) was adopted as the trial function, and best fitting was obtained with *a*, *b*, *c*, and *d* equal to 0.60, 0.14, 0.25, and −0.83, respectively.

abscissa z after probe deconvolution according to Eqs. (21) and (22). The deconvoluted curves are compared with $\alpha_c(z_0)$ and $OI(z_0)$ profiles experimentally detected by the confocal probe. Unlike the oxidation profile, for which the deconvoluted magnitude and morphology were substantially the same as those observed in the experimental (confocal) trend [$OI(z) \cong OI(z_0)$; see Fig. 16], the actual crystallinity gradient was found significantly steeper than that recorded by the confocal probe (see Fig. 15). The need of adopting a confocal probe configuration and the role of a mathematical probe deconvolution is even more critical when one considers that no gradient could be detected in the immediate subsurface of the material by a normal probe configuration with full aperture of the optical pinhole. Taddei et al.[15] investigated UHMWPE hip prostheses by Raman spectroscopy using a ×20 lens and

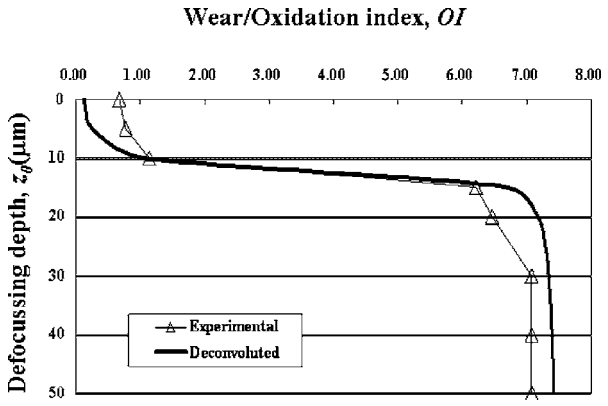

Fig. 16 Plots of wear index (related to oxidation index) distribution along the *in-depth z* axis as experimentally detected by the confocal probe and after mathematical probe deconvolution according to Eq. (20). In the calculation, Eq. (21) was adopted as the trial function, and best fitting was obtained with *a*, *b*, *c*, and *d* equal to 3.7, 2.4, 1.0, and −12.0, respectively.

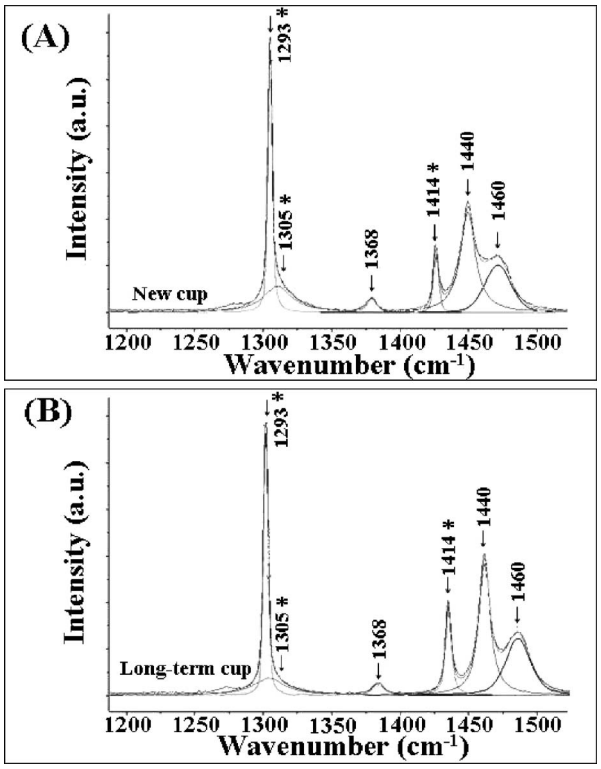

Fig. 17 Portions of Raman spectra investigated to calculate the oxidation index according to Eq. (6): (A) average spectrum collected on a new acetabular cup; and (B) average spectrum collected on the long-term exposed *in-vivo* acetabular cup. Spectral fitting by Gaussian/Lorentzian subbands is shown for both spectra and the salient bands used for assessing *OI* located with an asterisk.

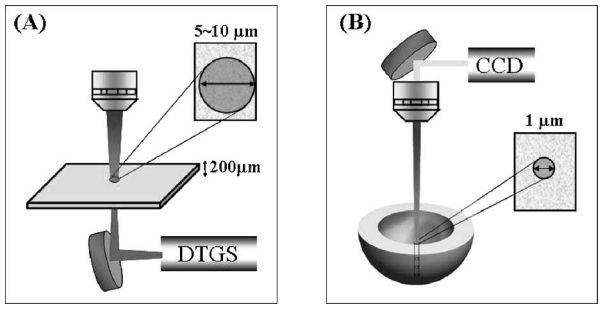

Fig. 18 Schematic drafts for (A) FTIR (destructive) and (B) confocal Raman (nondestructive) assessments of oxidation index in UHMWPE. The required sample thickness for FTIR assessment and lateral spatial resolutions are explicitly shown. DTGS and CCD abbreviations stand for deuterated triglycine sulfate and charge-coupled device, respectively.

without adopting a confocal probe configuration. Based on the outcomes of a previous investigation by Zerbi et al.,[27] these researchers argued that the Raman spectrum of UHMWPE was only contributed by the first 20 to 25 μm of material depth from the free surface. The present investigation shows that the *in-depth* spatial resolution adopted in the prior study, as well as in the majority of the Raman studies of polyethylene for artificial hip joints, is not suitable to fully detect the steep gradients of microstructural properties developed near the material surface on sterilization by γ-rays. We believe that these near-surface property gradients represent a separate piece of structural information which, besides millimeter-scale subsurface gradients, is also needed for a full understanding of the effect of γ-irradiation on the polyethylene structure. Using an optimized configuration of the confocal probe, aided by computational procedures to deconvolute the observed spectra, the full details of such microstructural distributions can be detected. This may help to reveal the actual origin of structural embrittlement in the immediate subsurface region, which ultimately leads to *in vivo* debris formation.

5 Conclusion

The (optical) probe response function for Raman bands of UHMWPE is systematically evaluated in both normal (pinhole full aperture) and confocal configurations of the optical probe. Based on these assessments, a suitable confocal probe configuration could be identified, which allowed us to greatly reduce laser penetration depth in the material. By shifting the focal plane of the confocal probe to different depths along the subsurface of the material, microstructural property gradients and wear-related degradation in retrieved UHMWPE acetabular cups could be systematically evaluated and compared to those present in a new cup as received from the maker after sterilization by γ-rays. This study clearly shows the suitability of confocal Raman spectroscopy for systematic wear studies of UHMWPE components of hip joints and for revealing through highly resolved imaging near-surface characteristics so far unexplored; however, it leaves unanswered important issues about the role of microstructural property gradients and *in-vivo* oxidation profiles on the wear response of the polymeric surface, and thus, on debris formation and the actual lifetime of the joint. This important issue definitely calls for systematic confocal Raman spectroscopic studies of joints subjected to different sterilization conditions before and after loading in advanced simulator devices.

6 Appendix

This section offers a quantitative explanation about the spectroscopic reliability of the present Raman measurements of *OI*, and shows the procedure followed for the empirical determination of Eq. (6) from a comparison between Fourier transformed infrared (FTIR) spectroscopy and Raman data. In addition to the considerations made in Sec. 3.1, it should be noted that the *OI* assessment in Eq. (6) employes Raman bands that are related to the unoxidized polyethylene structure. Therefore, *OI* can only be indirectly assessed through Eq. (6). Figures 17(A) and 17(B) show typical Raman spectra (both averaged over 100 locations), collected under the same acquisition conditions adopted for the images in Figs. 8–10. Data were collected on fresh (new cup) and degraded (long-term retrieval) UHMWPE, respectively. These figures also show the details of the spectroscopic fitting procedure adopted for data analysis. As can be seen, the spectral differences between the two materials are fine but clearly detectable, as follows: (I) a relative increase of the -CH_2- bond wagging band intensity I_{1414} with respect to the -CH_2- bond twisting band intensities ($I_{1293}+I_{1305}$) can be noticed in the degraded material; and (II) within the -CH_2- twisting vibration region 2, the band intensity I_{1305} is relatively higher in the new ma-

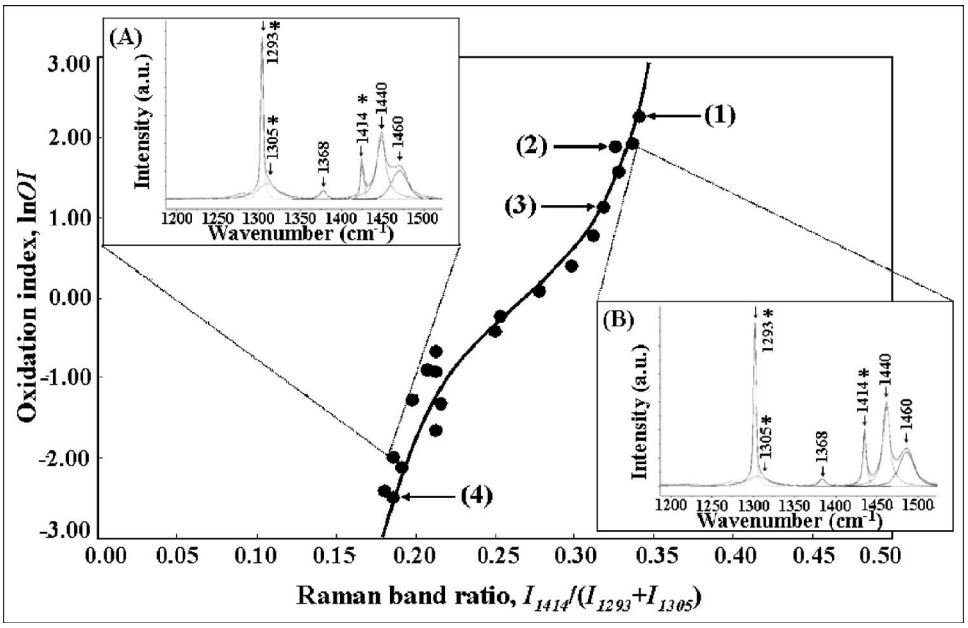

Fig. 19 Relationship between the Raman band ratio $I_{1414}/(I_{1293}+I_{1305})$ and *OI* (as determined by FTIR) in an increasingly oxidized UHMWPE sample. The dataset was least-square fitted to obtain Eq. (6) with a correlation factor $R^2=0.96$. In the insets, two typical Raman spectra (and related deconvoluted subbands) are shown for the low and high oxidation region of the plot, respectively. The bands employed for the indirect characterization of *OI* from the Raman spectrum are identified by an asterisk.

terial than in the degraded one. Note that both these features substantially contribute to the indirect determination of the *OI* value, according to Eq. (6). In this context, it is important to note that the fluorescence background in the present measurement conditions could be kept to a level sufficiently low to avoid obscuration of the vibrational bands of interest (emphasized by asterisk in Fig. 17). The empirical Eq. (6) was obtained by a least-square fitting routine on data collected on the same UHMWPE material at different oxidation levels by both FTIR and Raman spectroscopy. Aging of UHMWPE was made at 80°C up to 15 weeks, and a comparison was made with a similar sample held in inert atmosphere (evacuated package). Therefore, these data represent the outcome of "controlled" experiments performed under O_2 pressure versus inert atmosphere. The principles of the *OI* measurement are schematically shown for both techniques in Figs. 18(A) and 18(B), respectively. Note that unlike Raman, which is a fully nondestructive technique, FTIR spectroscopy should be performed in transmission mode and thus involves slicing of the sample into thin plates (5 to 10 μm in thickness). Figure 19 shows the relationship found on an increasingly oxidized sample between the Raman band ratio $I_{1414}/(I_{1293}+I_{1305})$ and *OI* (as determined by FTIR). The dataset can be least-square fitted to obtain Eq. (6) with a correlation factor $R^2=0.96$. In an attempt to make it available to the reader, the salient features of the spectra (as done before for data on new and long-term exposed cups in Fig. 17), two typical Raman spectra are shown in the inset as collected from the nonoxidized [Fig. 19(A)] and highly oxidized [Fig. 19(B)] regions of the plot in Fig. 19. No such spectroscopic features could be recognized on the sample held *in vacuo*. In addition, we also show in Fig. 20 the FTIR spectra collected on the UHMWPE material at different stages of aging (identified by arrows in the plot of Fig. 19). Sampling was made approximately in the same area where Raman spectra were collected. The lateral spot size in IR measurements was of several tens of microns. The *OI* values shown in Fig. 19 were obtained according to a standardized procedure given for UHMWPE to be used in surgical implants.[28]

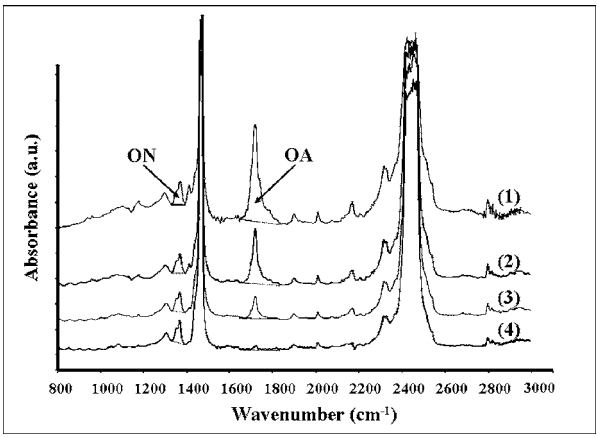

Fig. 20 IR spectra collected on a virgin UHMWPE cup after "controlled" experiments in an oxidizing atmosphere. These spectra correspond to the data points indicated by arrows in Fig. 19. *OI* was calculated according to ASTM standard[28] from the areas below the absorption curve as *OI*=OA/ON. The baseline curves are also explicitly indicated by broken lines.

Acknowledgments

The authors sincerely acknowledge Professor C. Jobe and Professor I. C. Clarke at the Department of Orthopaedics of Loma Linda University, California, for their enlightening dis-

cussions on the tribological behavior of UHMWPE both *in vivo* and in a joint simulator. An unknown reviewer is also greatly acknowledged for his/her important contribution in the discussion given on the validity of Eq. (6).

References

1. J. M. Kabo, J. S. Gebhard, G. Loren, and H. C. Amstutz, "In vivo wear of polyethylene acetabular components," *J. Bone Joint Surg. Br.* **75**, 254–258 (1993).
2. H. A. McKellop, P. Campbell, S. H. Park, T. P. Schmalzried, P. Grigoris, H. C. Amstutz, and A. Sarmiento, "The origin of submicron polyethylene wear debris in total hip arthroplasty," *Clin. Orthop.* **311**, 3–20 (1995).
3. I. C. Clarke, P. Campbell, and N. Kossowsky, "Debris-mediated osteolysis: a cascade phenomenon involving motion, wear, particulates, macrophage induction and bone lysis," in *Particulate Debris from Medical Implants: Mechanisms of Formation and Biological Consequences*, K. St. John, Ed. pp. 7–26, American Society for Testing and Materials, Philadelphia, PA (1992).
4. M. Goldman, R. Gronsky, G. G. Long, and L. Pruitt, "The effects of hydrogen peroxide and sterilization on the structure of ultra high molecular weight polyethylene," *Polym. Degrad. Stab.* **62**, 97–104 (1998).
5. M. Goldman, R. Gronsky, R. Ranganathan, and L. Pruitt, "The effects of gamma radiation sterilization and ageing on the structure and morphology of medical grade ultra high molecular weight polyethylene," *Polymer* **37**, 2909–2913 (1996).
6. S. Affatato, B. Bordini, C. Fagnano, P. Taddei, A. Tinti, and A. Toni, "Effects of the sterilization method on the wear of UHMWPE acetabular cups tested in a hip joint simulator," *Biomaterials* **23**, 1439–1446 (2002).
7. S. Affatato, G. Bersaglia, D. Emiliani, I. Foltran, P. Taddei, M. Reggiani, P. Ferrieri, and A. Toni, "The performance of gamma- and EtO-sterilized UHMWPE acetabular cups tested under severe simulator conditions. Part 2: wear particle characteristics with isolation protocols," *Biomaterials* **24**, 4045–4055 (2003).
8. S. Affatato, G. Bersaglia, M. Rocchi, P. Taddei, C. Fagnano, and A. Toni, "Wear behaviour of cross-linked polyethylene assessed in vitro under severe conditions," *Biomaterials* **26**, 3259–3267 (2005).
9. G. R. Strobl and W. Hagedorn, "Raman spectroscopic method for determining the crystallinity of polyethylene," *J. Polym. Sci., Polym. Phys. Ed.* **16**, 1181–1193 (1978).
10. F. Rull, A. C. Prieto, J. M. Casado, F. Sobron, and H. G. M. Edwards, "Estimation of crystallinity in polyethylene by Raman spectroscopy," *J. Raman Spectrosc.* **24**, 545–550 (1993).
11. C. C. Nylor, R. J. Meier, B. J. Kip, K. P. J. Williams, S. M. Mason, N. Conroy, and D. L. Gerrard, "Raman spectroscopy employed for the determination of the intermediate phase in polyethylene," *Macromolecules* **28**, 2969–2978 (1995).
12. B. Yeom, Y. J. Yu, H. A. McKellop, and R. Salovey, "Profile of oxidation in irradiated polyethylene," *J. Polym. Sci., Part A: Polym. Chem.* **36**, 329–339 (1998).
13. S. M. Kurtz, O. K. Muratoglu, F. J. Buchanan, B. Currier, R. Gsell, F. W. Shen, and S. S. Yau, "Interlaboratory studies to determine optimal analytical methods for measuring the oxidation index of UHMWPE," *Biomaterials* **22**, 2875–2881 (2001).
14. D. H. Chenery, "Detection of peroxy species in ultra-high-molecular-weight polyethylene by Raman spectroscopy," *Biomaterials* **18**, 415–419 (1997).
15. P. Taddei, S. Affatato, C. Fagnano, B. Bordini, A. Tinti, and A. Toni, "Vibrational spectroscopy of ultra-high molecular weight polyethylene hip prostheses: influence of the sterilization method on crystallinity and surface oxidation," *J. Mol. Struct.* **613**, 121–129 (2002).
16. M. Kyomoto, Y. Miwa, and G. Pezzotti, "Raman spectroscopic evaluation of UHMWPE for artificial hip joints," *J. Jpn. Soc. Replacement Arthro.* **35**, 79–80 (2005).
17. Z. Bartczak, "Influence of molecular parameters on high-strain deformation of polyethylene in the plane-strain compression. Part II. Strain recovery," *Polymer* **46**, 10339–10354 (2005).
18. L. Costa, M. P. Luda, L. Trossarelli, E. M. Brach del Prever, M. Crova, and P. Gallinaro, "Oxidation in orthopaedic UHMWPE sterilized by gamma-radiation and ethylene oxide," *Biomaterials* **19**, 659–668 (1998).
19. D. M. Lipkin and D. R. Clarke, "Sample-probe interactions in spectroscopy: Sampling microscopic property gradients," *J. Appl. Phys.* **77**, 1855–1863 (1995).
20. A. Atkinson and S. C. Jain, "Spatially resolved stress analysis using Raman spectroscopy," *J. Raman Spectrosc.* **30**, 885–891 (1999).
21. A. Chapiro, *Radiation Chemistry of Polymeric Systems*, Interscience, New York (1962).
22. V. Premnath, W. H. Harris, M. Jasty, and E. W. Merrill, "Gamma sterilization of UHMWPE articular implants: an analysis of the oxidation problem. Ultra high molecular weight poly ethylene," *Biomaterials* **17**, 1741–1753 (1996).
23. S. K. Bhateja, E. H. Andrews, and S. M. Yarbrough, "Radiation induced crystallinity changes in linear polyethylene: long-term aging effects," *Eur. Polym. J.* **21**, 739–750 (1989).
24. P. Eyerer, M. Kurth, H. A. McKellop, and T. Mittlmeier, "Characterization of UHMWPE hip cups run on joint simulators," *J. Biomed. Mater. Res.* **21**, 275–291 (1987).
25. P. Eyerer and Y. C. Ke, "Property changes of UHMW polyethylene hip cup endoprostheses during implantation," *J. Biomed. Mater. Res.* **18**, 1137–1151 (1984).
26. V. Premnath, A. Bellare, E. W. Merrill, M. J. Jasty, and W. H. Harris, "Molecular rearrangements in ultra high molecular weight polyethylene after irradiation and long-term storage in air," *Polymer* **40**, 2215–2229 (1999).
27. G. Zerbi, G. Gallino, N. Del Fanti, and L. Baini, "Structural depth profiling in polyethylene films by multiple internal reflection infrared spectroscopy," *Polymer* **30**, 2324–2327 (1989).
28. ASTM International Designation: F 2102-01$^{\varepsilon 1}$, "Standard guide for evaluating the extent of oxidation in ultra-high-molecular-weight polyethylene fabricated forms intended for surgical implants," in *Annual Book of ASTM Standards*, ASTM International, West Conshohocken, PA, pp. 1187–1190, Vol. 14.02 (2001).